Degenerate photons from a cryogenic spontaneous parametric down-conversion source

Nina Amelie Lange,* Timon Schapeler, Jan Philipp Höpker, Maximilian Protte, and Tim J. Bartley
Department of Physics and Institute for Photonic Quantum Systems, Paderborn University, Warburger Strasse 100, 33098 Paderborn, Germany

(Received 31 March 2023; accepted 12 July 2023; published 1 August 2023)

We demonstrate the generation of degenerate photon pairs from spontaneous parametric down-conversion in titanium-indiffused waveguides in lithium niobate at cryogenic temperatures. Since the phase matching cannot be temperature tuned inside a cryostat, we rely on a precise empirical model of the refractive indices when fabricating a fixed poling period. We design the phase-matching properties of our periodic poling to enable signal and idler photons at 1559.3(6) nm and characterize the indistinguishability of our photons by performing a Hong-Ou-Mandel interference measurement. Despite the effects of photorefraction and pyroelectricity, which can locally alter the phase matching, we achieve cryogenic indistinguishable photons within 1.5 nm of our design wavelength. Our results verify sufficient understanding and control of the cryogenic nonlinear process, which has wider implications when combining quasi-phase-matched nonlinear optical processes with other cryogenic photonic quantum technologies, such as superconducting detectors.

DOI: 10.1103/PhysRevA.108.023701

I. INTRODUCTION

Spontaneous parametric down-conversion (SPDC) under ambient conditions is a well-established technique for the generation of quantum light, such as heralded single photons [1], entangled photon pairs [2], and squeezed states [3]. Integrated SPDC in particular benefits from high conversion efficiencies and the propagation of photon pairs into well-defined waveguide modes [4,5]. This allows for the combination of integrated SPDC with other components to manipulate and detect the photons on a single chip [6–9]. In order to set up a fully integrated circuit including an SPDC source, two major challenges need to be overcome. On the one hand, integrated pump suppression together with integrated detection remains challenging [10,11]. On the other hand, all components must be compatible in their operating conditions [7].

In this work we address the second issue by adapting SPDC to the challenging operating conditions of superconducting detectors. Superconducting nanowire single-photon detectors (SNSPDs) provide detection efficiencies close to unity [12–14], low dark-count rates [15], and high timing resolution [16]. However, they must be operated below their critical temperature, and therefore require cryogenic operation [17]. To combine integrated SPDC together with high-performance SNSPDs, cryogenic SPDC becomes indispensable. Moreover, understanding how nonlinear processes can be designed to operate under cryogenic conditions is critical not just for nonlinear quantum light sources, but also for frequency conversion of other cryogenic photonic technologies [18].

We have recently shown the proof-of-principle functionality of cryogenic integrated type-II SPDC in titanium-indiffused lithium niobate waveguides [19]. While our SPDC source remained fully functional after changing the temperature by two orders of magnitude, there was a large shift in the phase-matching properties. Understanding the temperature-dependent changes in the SPDC process is important to predict and customize the nonlinear interaction at cryogenic temperatures. Here we demonstrate that we can achieve cryogenic degeneracy by tailoring the phase-matching properties of the nonlinear waveguide. We optimize the poling period to overlap the wavelengths of signal and idler in the telecom *C* band. We demonstrate the indistinguishability by characterizing the joint spectral intensity and performing a Hong-Ou-Mandel (HOM) interference measurement.

II. TEMPERATURE DEPENDENCE OF SPDC

The spectral properties of the signal and idler are determined by energy and momentum conservation, in practice described by the spectral distribution of the pump beam and the phase-matching function [20]. In general, the desired signal and idler wavelengths are often not phase matched because of the dispersion of the nonlinear crystal. Efficient interaction of a particular wavelength combination can be achieved by periodic inversion of the spontaneous polarization, also known as quasi-phase-matching [21]. While the pump distribution is independent of the waveguide temperature, quasi-phase-matching relies on the crystal dispersion, the length of the poled region, and the poling period. All three parameters are temperature dependent and need to be considered when investigating signal and idler properties under cryogenic operation.

Degenerate SPDC can be understood as the reverse process of classical second-harmonic generation (SHG) [22]. As a preliminary characterization, we thus start by performing an SHG measurement to determine the phase-matched wavelength, which is equal to the degenerate signal and idler wavelength.

*nina.amelie.lange@upb.de

The generated SHG power P_{SHG} at temperature T scales with the phase mismatch of the interacting fields Δk and the effective length of the poled region L as [23]

$$P_{\mathrm{SHG}}(T) \propto \mathrm{sinc}^2\left(\frac{\Delta k(T)L(T)}{2}\right). \tag{1}$$

The phase mismatch for a type-II process can be described by

$$\Delta k(T) = 2\pi\left(\frac{\Delta n(\lambda_{\mathrm{p}}, T)}{\lambda_{\mathrm{p}}} - \frac{1}{\Lambda(T)}\right), \tag{2}$$

with $\Delta n(\lambda_{\mathrm{p}}, T) = 2n_{\mathrm{TE}}(\lambda_{\mathrm{p}}/2, T) - n_{\mathrm{TE}}(\lambda_{\mathrm{p}}, T) - n_{\mathrm{TM}}(\lambda_{\mathrm{p}}, T)$ combining the temperature-dependent effective refractive indices n of the TE- or TM-polarized modes, pump wavelength λ_{p}, and poling period Λ. Under ambient conditions, the temperature dependence is used to tune the phase matching, but this method is incompatible with cryogenic operation. Therefore, we require precise knowledge of the desired poling period at low temperatures, which is fixed during fabrication.

We can describe our waveguide dispersion by applying Sellmeier equations for bulk lithium niobate [24,25], which are extrapolated for temperatures below room temperature. Furthermore, we include the estimated increase in the effective refractive indices due to the titanium indiffusion, to account for our waveguide geometry. This is done by using a commercial mode solving software (RSoft FemSIM), which is based on the finite-element method (for details, see [18]). The changes in the length of the poled region and poling period are given by the thermal contraction of lithium niobate, for which empirical data for temperatures down to 60 K are available [26]. For temperatures below 60 K, we assume the length to be unchanged, since the thermal expansion coefficient goes to zero at 0 K.

The extrapolation of the effective refractive indices introduces an uncertainty of our simulations. We address this problem by applying an additional experimentally determined correction to the refractive index data, using the method shown in [18]. By performing a stepwise cooldown of waveguides with five different poling periods and observing the shift in the phase-matched SHG wavelength, we can add an empirical correction to the phase-matching function to more accurately describe the change in the spectral properties. This is done by modifying Eq. (2) with $\Delta n(\lambda_{\mathrm{p}}, T) \rightarrow \Delta n(\lambda_{\mathrm{p}}, T) + \delta n(T)$, where $\delta n(T)$ is a temperature-dependent fifth-order polynomial function. The measured wavelength shifts for the five waveguides, together with the uncorrected and corrected simulation, are shown in Fig. 1. While both theoretical models describe the wavelengths well around room temperature, the empirical correction is required to provide an accurate description of the cryogenic SHG wavelength. Building on this, a thorough characterization of the cryogenic waveguide dispersion could be beneficial to further improve the precision of our model [27]. Using our modification, we choose a poling period of 8.81 μm to achieve cryogenic degeneracy in the telecom C band.

III. CHARACTERIZING CRYOGENIC PHASE MATCHING

We fabricate our waveguide sample including periodic poling by using a laser lithography tool. The waveguide structures are defined by titanium stripes which are indiffused into

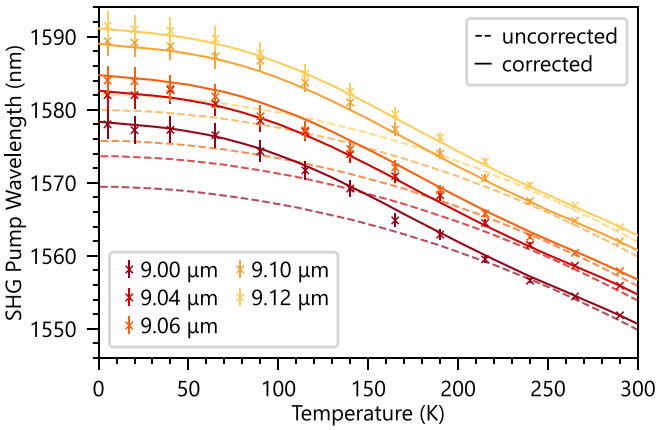

FIG. 1. Shift in the temperature-dependent phase-matched SHG pump wavelength for five different poling periods measured in a stepwise cooldown. The dashed lines show the uncorrected simulation and the solid lines represent the corrected simulation which includes the empirical correction term.

z-cut congruently grown lithium niobate. Afterward, the electrode patterns for the poling process are written and used to periodically invert the crystal polarization. For the waveguide investigated in this work, we choose a poling period of 8.81 μm and a length of 24.3(2) mm. According to our simulations, we expect the phase-matched wavelength for the chosen poling period to be $\lambda_{\mathrm{pm,theor}} = 1558.1$ nm at a temperature of 6.4 K, which is the base temperature of our cryostat. This means that we expect degenerate SPDC photons centered at this wavelength, when the cryogenic process is pumped at approximately 779 nm.

A. Cryogenic second-harmonic generation measurements

The experimental setup to detect the SHG signal is shown in Fig. 2. The waveguide is placed inside a free-space coupled cryostat, which provides direct access to the waveguide end facets through transparent windows. The laser beam is coupled to the waveguide using two aspheric lenses, equipped with an antireflection coating, placed outside the cryostat. The SHG process is pumped with a continuous-wave laser source, which can be tuned in the range from 1440 nm to 1640 nm. The optical pump power is set to 22.0(01) mW. The laser is followed by a half waveplate to set the input polarization. The unconverted pump light is filtered by a shortpass filter and the SHG power is then detected with a power meter.

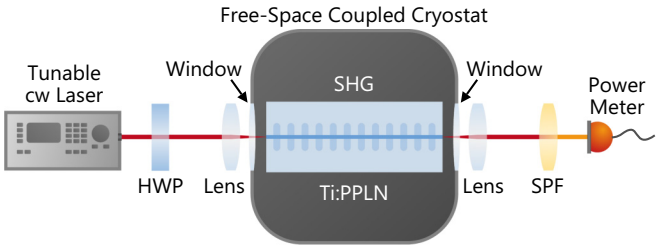

FIG. 2. Experimental setup to measure the SHG spectrum of the cryogenic waveguide, placed inside a free-space coupled cryostat: HWP, half waveplate; Ti:PPLN, titanium-indiffused periodically poled lithium niobate; and SPF, shortpass filter.

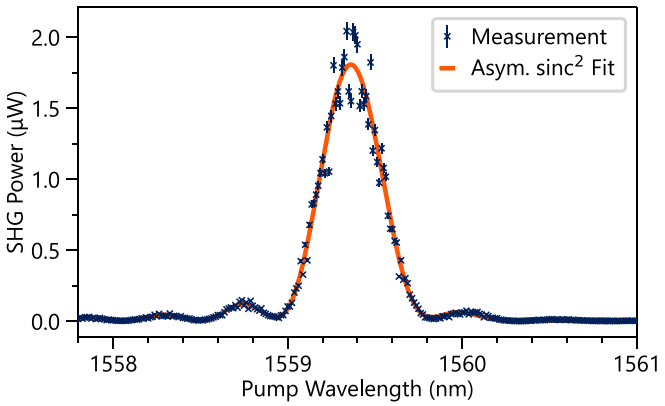

FIG. 3. Measured data for the cryogenic SHG power over the pump wavelength. The asymmetric fit function considers a nonuniform refractive index distribution along the waveguide direction. The error bars correspond to an uncertainty of ±3%, as specified for the power meter used.

B. Analysis of the spectral results

We tune the pump wavelength while measuring the generated SHG power. The measurement data are presented in Fig. 3. According to Eq. (1), the phase-matching function is expected to show a sinc^2 shape. This description holds for an ideal process, while the actual interaction inside the lithium niobate waveguide can be altered by fabrication imperfections, pyroelectricity, and photorefraction [28]. The pyroelectric and photorefractive effects can lead to an accumulation of electric charges inside the waveguide region. The interplay of those effects can cause localized perturbations of the refractive indices due to the electro-optic effect [18], induced by temperature changes during the cooldown [29], or high optical power [30].

Our measured spectrum is indeed very close to the ideal sinc^2 function; the overlap is 99.9%. We can more accurately model the exact shape by considering a nonuniform refractive index distribution along the waveguide. This results in a very slight asymmetry of the sinc^2 function, which takes into account imperfections of the phase matching. For this analysis we follow the procedure presented in [18]. The fit reveals an effective length of $L_{\mathrm{eff}} = 18.8(3)$ mm, corresponding to 77.4(14)% of the total waveguide length. This means that the phase-matching condition is satisfied for this fraction of our waveguide, which demonstrates precise fabrication of a uniform poling period.

In addition to the effective length of the waveguide, we can extract the phase-matched wavelength $\lambda_{\mathrm{pm,meas}} = 1559.36(2)$ nm from the SHG measurement. The error of this value is given by the absolute wavelength accuracy of our laser source. In comparison to the theoretical value, the measured wavelength is slightly higher. Various factors can contribute to this discrepancy. On the one hand, our simulation is based on an empirical refractive index correction term, which induces experimental uncertainty. On the other hand, perturbations in the refractive indices can induce an additional shift of the phase-matched wavelength. In fact, the phase-matched wavelength changed to $\lambda_{\mathrm{pm,meas}} = 1558.60(2)$ nm in a second cooldown, which was performed more than a month later. Pyroelectric charges gather randomly at different locations inside the crystal. Resulting localized refractive index perturbations, which overlap with the waveguide, alter the phase matching. The dynamics in the temperature-dependent phase matching was observed before, indicating the buildup and discharge of pyroelectric charges on different timescales [18]. Recent work has further shown a clear correlation between discontinuities in the generated charge flow inside the waveguide and variations in the birefringence [31]. Since the charge mobility decreases for cryogenic operation, we expect a carrier freeze-out, which means that remaining charges cannot discharge and result in a permanent phase-matching modification while the crystal is kept cold. Hence, a slight variation in the phase matching can arise for every cooldown cycle. We thus assume spontaneous changes in the accumulating charges to be the primary cause of the discrepancy between experiment and theory. Nevertheless, the experimental SHG wavelengths are indeed very close to our theoretical result, which shows accurate fabrication and good predictability of the phase-matching behavior under cryogenic conditions.

IV. MEASURING CRYOGENIC SPDC PHOTONS

Following the SHG characterization, we use the setup shown in Fig. 4(a) to pump the SPDC process. We pump the cryogenic SPDC with the SHG signal generated in a bulk periodically poled MgO-doped lithium niobate crystal. This crystal is pumped by a pulsed infrared laser with a repetition rate of 80 MHz, a wavelength of 1556.4(2) nm, and a bandwidth of 11.81(2) nm. The SHG crystal is temperature controlled to allow fine adjustment of the generated SHG wavelength within a few nanometers. This way, we set the pump wavelength to fit our phase-matched wavelength. We use a $4f$ line to set the spectral bandwidth to 0.73(5) nm. Shortpass filters in front of the cryostat filter out the residual infrared components, before pumping the SPDC chip. The signal and idler photons are filtered by longpass filters and separated by a polarizing beam splitter.

We start by investigating the spectral properties with a home-built scanning-grating spectrometer setup shown in Fig. 4(b). One spectrometer is placed in each path. The wavelength components of the signal or idler photons are separated by a blazed grating, before part of the spectrum is coupled into a polarization-maintaining single-mode fiber. Further details on the spectrometer setup design can be found in the Supplemental Material of [19]. For the spectral measurements, the spectrometers are directly connected to superconducting nanowire single-photon detectors. The detectors are positioned in a separate cryostat. A time-tagging module is used to record the coincidence counts of the two detectors.

A. Joint spectrum of the signal and idler

We measure the joint spectral intensity (JSI) of signal and idler photons by scanning the two gratings and detecting the coincidence counts. For this measurement, we set the optical power of the pump beam to 133(1) μW and the integration time for every measurement point to 4 s. The measurement data are shown in Fig. 5. We present the JSI

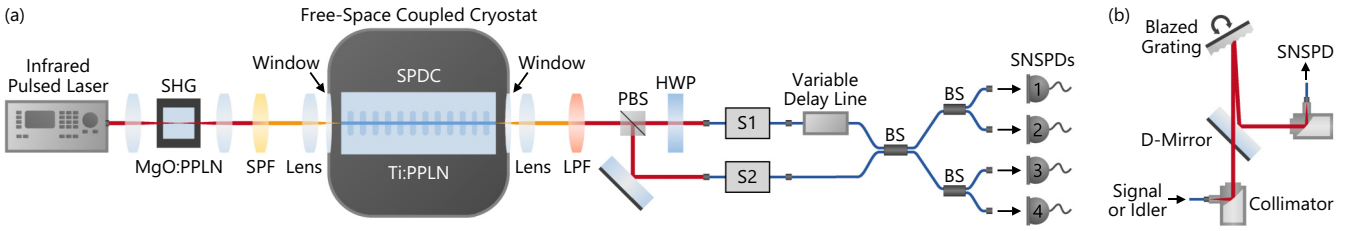

FIG. 4. (a) Experimental setup to perform the Hong-Ou-Mandel interference measurement of the cryogenic SPDC source. (b) One scanning-grating spectrometer setup is inserted into each path in order to spectrally filter signal and idler. The following denotations are used: MgO:PPLN (Ti:PPLN), MgO-doped (titanium-indiffused) periodically poled lithium niobate; SPF, shortpass filter; LPF, longpass filter; (P)BS, (polarizing) beam splitter; HWP, half waveplate; and S1 and S2, spectrometers 1 and 2.

together with the marginal spectra of the signal and idler, which correspond to the projection on the two axes. We apply a Gaussian fit to the marginals to obtain the central wavelengths and bandwidths. The shape of the signal spectrum deviates from a Gaussian shape, which is caused by a slight asymmetry of our pump spectrum, after filtering with the $4f$ line. Nevertheless, the fit matches the data well enough to provide the main parameters. The signal spectrum has a central wavelength of $\lambda_s = 1559.3(5)$ nm and a bandwidth of $\Delta\lambda_s = 6.33(12)$ nm, while the idler spectrum is centered at the same wavelength $\lambda_i = 1559.3(6)$ nm with a smaller bandwidth of $\Delta\lambda_i = 3.26(3)$ nm. The uncertainties of the central wavelengths correspond to the transmission bandwidths of the spectrometers, and the errors of the marginal bandwidths arise from the uncertainty in the spectrometer calibration and the error of the Gaussian fit. For the signal and idler spectra, we obtain a difference in the bandwidths. This is due to the angular orientation of the JSI, which is fundamental to the phase matching and thus the material properties of lithium niobate. The spectral purity of our photons is limited by correlations in the signal and idler wavelengths. We analyze these correlations by performing a Schmidt decomposition [32],

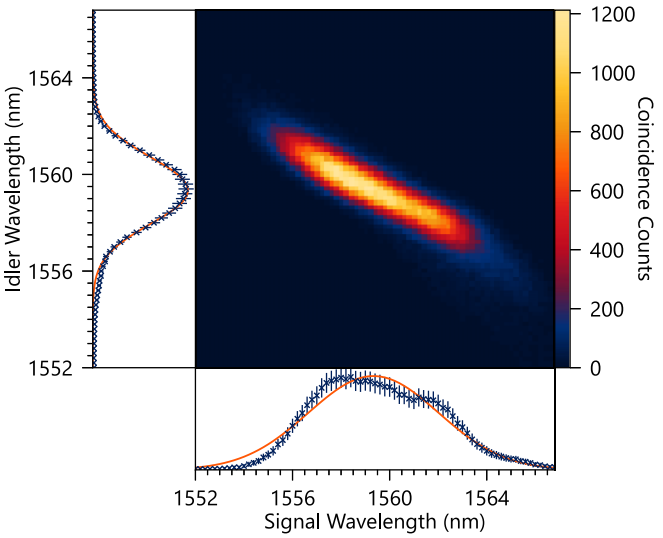

FIG. 5. Measured joint spectral intensity of the signal and idler photons, together with the marginal spectra. Here the error bars correspond to Poisson errors and a Gaussian fit is applied to the marginal data.

which results in a Schmidt number of 2.72, corresponding to a spectral purity of 0.37. The purity can be increased by spectrally filtering in the signal and idler arm, as we do for the HOM interference measurement (see Sec. IV C).

The measurement of the JSI shows that the signal and idler wavelengths are identical and very close to the measured phase-matched wavelength for SHG. In comparison to the SHG spectrum, the JSI was measured about one week later, during which the waveguide was kept at cryogenic temperatures. This clearly verifies that in spite of the buildup of pyroelectric charges, which can disturb the phase matching during temperature change, the SPDC source allows for stable operation at a constant temperature.

B. SPDC source performance

The experimental setup is further modified to measure the source brightness B, the Klyshko efficiency η_{Klyshko} [33], and the heralded second-order correlation function $g_h^{(2)}(0)$. For the first two measurements, the spectrometers are removed and the signal and idler photons are each connected to an SNSPD. For the $g_h^{(2)}(0)$ measurement, a 50:50 fiber beam splitter is added to the idler path to characterize the photon-number statistics. The SPDC chip is pumped with an optical power of 66.1(1) μW, corresponding to a low photon-pair generation probability of 0.01.

We define the source brightness as $B = C_{si}/P_{trans}$, where C_{si} is the signal and idler coincidence rate and P_{trans} is the transmitted pump power. Our source has a brightness of $B = 6.0(3) \times 10^5$ pairs/s mW. The combined Klyshko efficiency for both paths is given by $\eta_{\text{Klyshko}} = \sqrt{C_{si}^2/C_s C_i}$, with C_s and C_i the single count rates of the signal and idler. We obtain an efficiency of $\eta_{\text{Klyshko}} = 13.62(8)\%$. At the same time we measure a low $g_h^{(2)}(0)$ value of $g_h^{(2)}(0) = 0.017(2)$. The heralded autocorrelation function is given by $g_h^{(2)}(0) = C_{i_1 i_2 s} C_s / C_{i_1 s} C_{i_2 s}$, where $C_{i_1 s}$ and $C_{i_2 s}$ are the coincidences of the two idler paths with the signal photons, respectively, and $C_{i_1 i_2 s}$ are the threefold coincidences. Our result for the heralded $g_h^{(2)}(0)$ is well below the threshold for a two-photon Fock state [$g_h^{(2)}(0) = 0.5$], which clearly verifies cryogenic single-photon generation.

C. Demonstration of indistinguishability

Having shown that our SPDC source generates single photons at cryogenic temperatures and the signal and idler spectra

overlap very well, we demonstrate the indistinguishability in the other degrees of freedom. For this purpose, we perform a Hong-Ou-Mandel interference measurement by using the experimental setup as shown in Fig. 4(a). The spectrometers S1 and S2 are connected to the signal and idler path, acting as spectral bandpass filters. This allows us to increase the spectral purity and therefore the indistinguishability of our photon source. Our filters have slightly different transmission bandwidths of $\Delta\lambda_s = 0.96(3)$ nm and $\Delta\lambda_i = 1.12(3)$ nm due to experimental imperfections in the home-built setups. We adjust the spectral filters by setting one filter to the central wavelength of the marginals and fine-tuning the other grating to maximize the spectral overlap. However, small differences in the grating position and spectral bandwidth will limit the visibility of our HOM dip. We use a type-II SPDC process, which results in orthogonal polarization of the signal and idler. Therefore, a half waveplate is placed in front of one spectrometer to rotate the signal polarization by 90°. To guarantee stable polarization, all fibers used in this setup are polarization maintaining. Following the spectrometer, we add a fiber-coupled delay line to tune the temporal delay between the signal and idler, before both photons meet at the subsequent 50:50 beam splitter. After this interference beam splitter, both paths are split again with another 50:50 beam splitter, before each signal is detected with an SNSPD. We measure the twofold coincidence rates between all four detectors to gain information about the photon statistics in each arm. The temporal delay $\Delta\tau$ is tuned in steps of 1 ps and the measurement of the coincidence rates, together with the single count rates, is shown in Fig. 6. We apply Gaussian fit functions to all coincidence measurements to normalize the two axes. For clarity, only the average fits for the peak and dip in the coincidences are shown in Fig. 6.

For perfect temporal overlap ($\Delta\tau = 0$) we clearly see a peak in the coincidence rates C_{12} and C_{34}. Simultaneously, there is a significant dip in the twofold coincidences between the different interference paths. The dip goes below the threshold of 0.5, which verifies bunching of the signal and idler photons. We calculate the HOM visibility of the photons from the sum of all coincidence counts which appear between different interference paths $C = C_{13} + C_{14} + C_{23} + C_{24}$. The visibility is thus defined by $V = 1 - C(\Delta\tau = 0)/C(\Delta\tau \to \infty)$, which gives us a visibility of $V = 66.3(5)\%$. This visibility is mainly limited by imperfections in the spectral filtering. We determine an upper limit by calculating the spectral overlap of the signal and idler photons. The filtered spectra are obtained by applying the transmission spectra of our spectrometers to the marginals. They show a spectral overlap of 76.3%. A further decrease of the visibility can be explained by an imperfect splitting performance of the polarizing beam splitter (PBS). This is caused, on the one hand, by the specified polarization extinction ratio and, on the other hand, by a slight misalignment of the angle between the waveguide chip and the PBS. These limitations cause a small fraction of the signal and idler photons to take the incorrect path. As a consequence, the photon pair enters the interference beam splitter at the same input port, which affects the coincidence measurement statistics. We assume that the visibility is further limited by slight differences in the alignment of polarization after passing through the PBS and in the spatial mode after filtering with our spectrometers. Higher visibility might be achieved in future experiments by using identical bandpass filters and an additional half waveplate in front of the PBS. Nevertheless, we can clearly show the bunching of the signal and idler in our HOM interference measurement and therefore we can obtain degenerate photons from our cryogenic single-photon source.

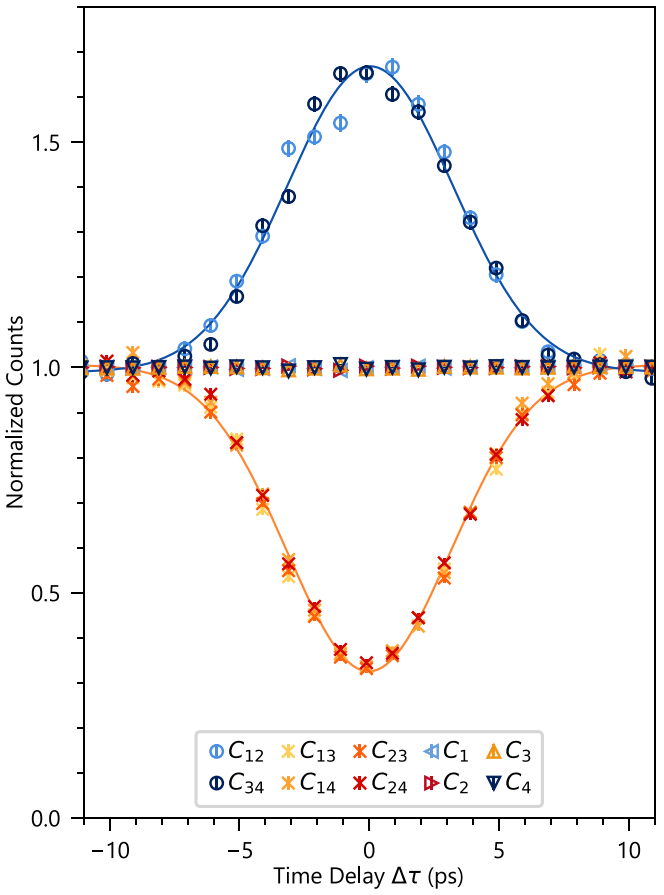

FIG. 6. Hong-Ou-Mandel interference dip measurement of the cryogenic SPDC photons. The plot shows the normalized count rates for all twofold coincidences and single counts of the SNSPDs shown in Fig. 4. We represent coincidences between two detectors within one beam-splitter path by circles, coincidences between detectors in different paths by crosses, and the single counts by triangles. The error bars correspond to Poisson errors and the solid lines represent a Gaussian fit for the peak and dip, respectively.

V. CONCLUSION

Cryogenic SPDC is a crucial component for integrated quantum optics with superconducting detectors. Our Hong-Ou-Mandel measurement shows that we have successfully generated degenerate photon pairs in the telecom *C* band from a cryogenic integrated SPDC source. When operated under ambient conditions, modifying the phase matching using temperature tuning is a common method to achieve degeneracy, but temperature tuning cannot be used for cryogenic operation. We have demonstrated a precise theoretical model to predict the poling period which is required to achieve efficient phase matching for the cryogenic degenerate process. This is indispensable since the periodic poling is the only

parameter we can use to tune the phase matching in a cryostat and it needs to be defined before fabrication. Despite the fact that no absolute values for the cryogenic effective refractive indices are available and that pyroelectricity and photorefraction can locally perturb the phase matching, our experimental wavelength is within 1.5 nm of our design. Moreover, our phase-matching function is very close to the ideal sinc^2 shape. We thus show accurate and uniform fabrication of the poling period, maintained under cryogenic conditions, which is significant to realize efficient and customized frequency conversion devices for future cryogenic integration. Our results demonstrate reliable control of the cryogenic nonlinear interaction, which should help in the realization of fully integrated cryogenic quantum circuits to promote the proliferation of quantum technologies.

ACKNOWLEDGMENTS

We acknowledge financial support from the Deutsche Forschungsgemeinschaft (Grant No. 231447078–TRR 142) and the Bundesministerium für Bildung und Forschung (Grant No. 13N14911), as well as the European Union (ERC, Project QuESADILLA, Grant No. 101042399). Views and opinions expressed are however those of the author(s) only and do not necessarily reflect those of the European Union or the European Research Council. Neither the European Union nor the granting authority can be held responsible for them.

[1] C. K. Hong and L. Mandel, Experimental Realization of a Localized One-Photon State, Phys. Rev. Lett. **56**, 58 (1986).

[2] P. G. Kwiat, K. Mattle, H. Weinfurter, A. Zeilinger, A. V. Sergienko, and Y. Shih, New High-Intensity Source of Polarization-Entangled Photon Pairs, Phys. Rev. Lett. **75**, 4337 (1995).

[3] L.-A. Wu, H. J. Kimble, J. L. Hall, and H. Wu, Generation of Squeezed States by Parametric Down Conversion, Phys. Rev. Lett. **57**, 2520 (1986).

[4] G. Fujii, N. Namekata, M. Motoya, S. Kurimura, and S. Inoue, Bright narrowband source of photon pairs at optical telecommunication wavelengths using a type-II periodically poled lithium niobate waveguide, Opt. Express **15**, 12769 (2007).

[5] O. Alibart, V. D'Auria, M. De Micheli, F. Doutre, F. Kaiser, L. Labonté, T. Lunghi, É. Picholle, and S. Tanzilli, Quantum photonics at telecom wavelengths based on lithium niobate waveguides, J. Opt. **18**, 104001 (2016).

[6] J.-H. Kim, S. Aghaeimeibodi, J. Carolan, D. Englund, and E. Waks, Hybrid integration methods for on-chip quantum photonics, Optica **7**, 291 (2020).

[7] J. Wang, F. Sciarrino, A. Laing, and M. G. Thompson, Integrated photonic quantum technologies, Nat. Photon. **14**, 273 (2020).

[8] G. Moody, V. J. Sorger, D. J. Blumenthal, P. W. Juodawlkis, W. Loh, C. Sorace-Agaskar, A. E. Jones, K. C. Balram, J. C. F. Matthews, A. Laing *et al.*, 2022 roadmap on integrated quantum photonics, J. Phys. Photon. **4**, 012501 (2022).

[9] E. Pelucchi, G. Fagas, I. Aharonovich, D. Englund, E. Figueroa, Q. Gong, H. Hannes, J. Liu, C.-Y. Lu, N. Matsuda *et al.*, The potential and global outlook of integrated photonics for quantum technologies, Nat. Rev. Phys. **4**, 194 (2022).

[10] N. C. Harris, D. Grassani, A. Simbula, M. Pant, M. Galli, T. Baehr-Jones, M. Hochberg, D. Englund, D. Bajoni, and C. Galland, Integrated Source of Spectrally Filtered Correlated Photons for Large-Scale Quantum Photonic Systems, Phys. Rev. X **4**, 041047 (2014).

[11] C. M. Gentry, O. S. Magaña-Loaiza, M. T. Wade, F. Pavanello, T. Gerrits, S. Lin, J. M. Shainline, S. D. Dyer, S. W. Nam, R. P. Mirin, and M. A. Popović, *Conference on Lasers and Electro-Optics, San Jose, 2018* (Optica Publishing Group, Washington, DC, 2018), paper JTh4C.3.

[12] L. You, Superconducting nanowire single-photon detectors for quantum information, Nanophotonics **9**, 2673 (2020).

[13] D. V. Reddy, R. R. Nerem, S. W. Nam, R. P. Mirin, and V. B. Verma, Superconducting nanowire single-photon detectors with 98% system detection efficiency at 1550 nm, Optica **7**, 1649 (2020).

[14] J. Chang, J. W. N. Los, J. O. Tenorio-Pearl, N. Noordzij, R. Gourgues, A. Guardiani, J. R. Zichi, S. F. Pereira, H. P. Urbach, V. Zwiller *et al.*, Detecting telecom single photons with $(99.5^{+0.5}_{-2.07})\%$ system detection efficiency and high time resolution, APL Photon. **6**, 036114 (2021).

[15] J. Chiles, I. Charaev, R. Lasenby, M. Baryakhtar, J. Huang, A. Roshko, G. Burton, M. Colangelo, K. Van Tilburg, A. Arvanitaki, S. W. Nam, and K. K. Berggren, New Constraints on Dark Photon Dark Matter with Superconducting Nanowire Detectors in an Optical Haloscope, Phys. Rev. Lett. **128**, 231802 (2022).

[16] B. Korzh, Q.-Y. Zhao, J. P. Allmaras, S. Frasca, T. M. Autry, E. A. Bersin, A. D. Beyer, R. M. Briggs, B. Bumble, M. Colangelo *et al.*, Demonstration of sub-3 ps temporal resolution with a superconducting nanowire single-photon detector, Nat. Photon. **14**, 250 (2020).

[17] A. W. Elshaari, W. Pernice, K. Srinivasan, O. Benson, and V. Zwiller, Hybrid integrated quantum photonic circuits, Nat. Photon. **14**, 285 (2020).

[18] M. Bartnick, M. Santandrea, J. P. Höpker, F. Thiele, R. Ricken, V. Quiring, C. Eigner, H. Herrmann, C. Silberhorn, and T. J. Bartley, Cryogenic Second-Harmonic Generation in Periodically Poled Lithium Niobate Waveguides, Phys. Rev. Appl. **15**, 024028 (2021).

[19] N. A. Lange, J. P. Höpker, R. Ricken, V. Quiring, C. Eigner, C. Silberhorn, and T. J. Bartley, Cryogenic integrated spontaneous parametric down-conversion, Optica **9**, 108 (2022).

[20] W. P. Grice, A. B. U'Ren, and I. A. Walmsley, Eliminating frequency and space-time correlations in multiphoton states, Phys. Rev. A **64**, 063815 (2001).

[21] S. Tanzilli, H. De Riedmatten, H. Tittel, H. Zbinden, P. Baldi, M. De Micheli, D. B. Ostrowsky, and N. Gisin, Highly efficient photon-pair source using periodically poled lithium niobate waveguide, Electron. Lett. **37**, 26 (2001).

[22] C. Couteau, Spontaneous parametric down-conversion, Contemp. Phys. **59**, 291 (2018).

[23] R. W. Boyd, *Nonlinear Optics* (Academic, New York, 2008).
[24] G. J. Edwards and M. Lawrence, A temperature-dependent dispersion equation for congruently grown lithium niobate, Opt. Quantum Electron. **16**, 373 (1984).
[25] D. H. Jundt, Temperature-dependent Sellmeier equation for the index of refraction, n_e, in congruent lithium niobate, Opt. Lett. **22**, 1553 (1997).
[26] *Properties of Lithium Niobate*, edited by K. K. Wong (Institution of Engineering and Technology, Edison, 2002).
[27] M. Misiaszek, A. Gajewski, and P. Kolenderski, Dispersion measurement method with down conversion process, J. Phys. Commun. **2**, 065014 (2018).
[28] R. S. Weis and T. K. Gaylord, Lithium niobate: Summary of physical properties and crystal structure, Appl. Phys. A **37**, 191 (1985).
[29] J. Parravicini, J. Safioui, V. Degiorgio, P. Minzioni, and M. Chauvet, All-optical technique to measure the pyroelectric coefficient in electro-optic crystals, J. Appl. Phys. **109**, 033106 (2011).
[30] J. Rams, A. A. de Velasco, M. Carrascosa, J. Cabrera, and F. Agulló-López, Optical damage inhibition and thresholding effects in lithium niobate above room temperature, Opt. Commun. **178**, 211 (2000).
[31] F. Thiele, T. Hummel, N. A. Lange, F. Dreher, M. Protte, F. vom Bruch, S. Lengeling, H. Herrmann, C. Eigner, C. Silberhorn, and T. J. Bartley, Pyroelectric influence on lithium niobate during the thermal transition for cryogenic integrated photonics, arXiv:2306.12123.
[32] A. Ekert and P. L. Knight, Entangled quantum systems and the schmidt decomposition, Am. J. Phys. **63**, 415 (1995).
[33] D. N. Klyshko, Use of two-photon light for absolute calibration of photoelectric detectors, Sov. J. Quantum Electron. **10**, 1112 (1980).